A model for the prediction of thermal runaway in lithium–ion batteries

Bernardo J. Azuaje–Berbec´ı[a], H. Bulent Ertan¨[b,*]

[a]Atılım University, Department of Electrical and Electronics Engineering, Kızılcasar, Incek Go¨lbası, Go¨lbası, 06830, Ankara, Tu¨rkiye [b]Atılım University, Department of Mechatronics Engineering, Kızılcasar, Incek Go¨lbası, Go¨lbası, 06830, Ankara, Tu¨rkiye

Abstract

The increasing popularity of electric vehicles is driving research into lithium-ion batteries (LIBs). Thermal runaway (TR), a major exothermal process, is a serious obstacle to the safety of high-energy-density LIBs that has yet to be overcome. A reliable model is needed to predict thermal runaway (TR) conditions and prevent an uncontrolled cascade of chemical reactions. This study develops a multilayered electrochemical-thermal model for the commercially available 3 Ah LG HG2 NMC-811/SiC and 1.6 Ah pouch $LiFePO_4$ batteries, considering the effects of chemical reactions during TR. The proposed model is analyzed in detail and then validated against experimental results at ambient temperatures of 298.15 K and 338.15 K. The multilayered model is designed to predict working voltage, heat generation, temperature gradients, and the possibility of TR under various operating conditions and environmental temperatures. Results showed that the model predictions of voltage and temperature agree well with experimental data at various operating conditions. The model is then used to investigate the effect of high discharge-charge current levels on battery temperature, demonstrating a good prediction of TR during LIB cycling. The analysis presented here is promising to help identify conditions that can lead to TR and guide the safe design of battery management systems.

Keywords: Electrochemical–thermal model, NMC–811 Lithium-ion battery, LFP Lithium-ion battery, Heat generation, Thermal runaway.

1. Introduction

The International Energy Agency [1] projects that by 2030, electric vehicles (EVs) will account for 60% of car sales. This rising demand for EVs has spurred research into their components. The acceleration and top speed of an EV mostly depend on the motor. However, it is the battery pack that holds importance. The battery pack limits the performance of EVs and is prone to failure. The battery pack is prone to thermal runaway (TR), which can cause fire and explosions. Interest in predicting heat generation and temperature fields in a lithium-ion battery (LIB) has recently increased due to the potential of developing effective methods to prevent TR.

TR is a chain of exothermic reactions that causes the LIB's temperature to rise suddenly. Although LIBs are susceptible to TR, they are the main choice for battery packs as a rechargeable energy source. The increased active material content in highenergy-density LIBs, such as lithium nickel manganese cobalt oxide (NMC-811), makes them more susceptible to TR. The thermal instability of LIBs at high temperatures can lead to fire hazards. High temperatures can cause active materials in LIBs to decompose, leading to TR [2]. TR results from accumulated heat generation [3] and has an incubation period that is mainly determined by heating conditions [4]. Abusive conditions, including electrical, thermal, mechanical impact, and battery cell defects or aging, can lead to TR [5]. The temperature rise of a LIB is dependent on the heat generation rate produced at a specific operating condition, while its temperature after the battery is disconnected is dependent on the thermal time constant of the LIB. TR is a major concern in battery thermal safety research [6]. The increasing popularity of EVs poses a serious safety hazard to passengers due to the risk of TR in LIBs. In recent years, the number of LIB-related accidents has increased, with the majority occurring during the summer months (June-August) [7]. It is therefore essential to predict TR and warn passengers of the potential for LIB failure due to TR to avoid serious injuries or death.

Several empirical models have been used to predict the behavior of LIBs and their heat generation. The pseudo-two-dimensional (P2D) model [8] is a widely accepted physics-based model able to characterize the dynamics of LIBs. Significant research has been conducted to improve the prediction of temperature within LIBs using a multilayered domain approach. Alipour et al. [9] showed that temperature prediction accuracy increases with increasing layers in modeling as compared to traditional single-layer models. Li et al. [10] extended the P2D model to account for the arc length of the jelly roll and studied the temperature field of an 18650 LIB. The results suggest that polarization heat is dominant at lower discharge rates, whereas ohmic heat is dominant at higher discharge rates.

Recently, Rania et al. [11] showed that entropic heat cannot be ignored, as it represents approximately 50% of total heat generated for a 2/3C current rate and 39% for a 1C rate. Khalid et al. [12] argued that reversible heat generation strongly affects the temperature of the LIB during a charge and discharge cycle.

* Corresponding uthor
Email address:
ulent.ertan@atilim.edu.tr
(H. Bulent Ertan)¨

ɔclature

symbols

	Tab cross-section area (m^2)
	Frequency factor of electrolyte (1/s)
A	Frequency factor due to internal short circuit (1/s)
A_{ele}	Frequency factor of negative–electrolyte (1/s)
A_{isc}	Frequency factor of positive–electrolyte (1/s)
A_{ne}	Frequency factor of SEI decomposition (1/s)
A_{pe}	Battery capacity (C)
A_{sei}	Li^+ concentration in the liquid phase (mol/m^3)
C_{cell} c_l	Specific heat capacity (J/mol^2–K)
C_p c_s	Li^+ concentration in the solid phase (mol/m^3)
c_{max_S}	Max. Li^+ concentration in the solid phase (mol/m^3)
D_{eff}	Effective diffusion coefficient of Li^+ in the liquid phase (m^2/s)
D_s	Active material diffusion coefficient of Li^+ in the solid phase (m^2/s)
Ea_{ele}	Activation energy of electrolyte (J/mol)
Ea_{isc}	Activation energy due to internal short circuit (J/mol)
Ea_{ne}	Activation energy of negative–electrolyte (J/mol)
Ea_{pe}	Activation energy of positive–electrolyte (J/mol)
Ea_{sei}	Activation energy of SEI decomposition (J/mol)
F	Faraday's constant (C/mol)
$f_{\pm}$	Average molar activity coefficient
h	Heat transfer coefficient (W/m^2-K)
H_{ele}	Reaction heat of electrolyte (J/kg)
H_{isc}	Reaction heat due to internal short circuit (J/kg)
H_{ne}	Reaction heat of negative–electrolyte (J/kg)
H_{pe}	Reaction heat of positive–electrolyte (J/kg)
H_{sei}	Reaction heat of SEI decomposition (J/kg)
I_{app}	Total applied current (A)
i_l i_s	Electronic current density in the liquid phase (A/m^2)
j_0 j_{loc}	Electronic current density in the solid phase (A/m^2)
k_B L	Exchange current density (A/m^2)
m_{ele}	Local current density (A/m^2)
m_{ne}	Boltzmann constant (J/K)
m_{pe}	Tab length (m)
m_{sei}	Activation energy of C_{ele} Reaction
	order for C_{ne}
	Activation energy of C_{pe}
	Reaction order for C_{sei}

Q_{ele}	Electrolyte decomposition heat (W/m^3)
Q_{irr}	Irreversible heat generation rate (W/m^3)
Q_{isc}	Internal short circuit heat (W/m^3)
Q_{ne}	Anode–electrolyte decomposition heat (W/m^3)
Q_{ohm}	Ohmic heat generation (W/m^3)
Q_{pe}	Cathode–electrolyte decomposition heat (W/m^3)
Q_{rev}	Reversible entropic heat generation rate (W/m^3)
Q_{sei}	SEI decomposition heat (W/m^3)
Q_{tab}	Total heat loss on battery's tab (W/m^3)
R	Universal gas's constant (J/mol^2-K)
r	Radial distance into electrode's particles (m)
R_f	Surface–layer resistance (Ωm^2)
R_p	Particle radius^{D50} (m)
S_a	Specific surface area (1/m)
T	Temperature (K)
t_{+0}	Transfer number of Li^+
U_{eq}	Open circuit potential (V)
V_{cell}	Terminal voltage (V)
W_c	Carbon content per unit volume anode (kg/m^3)
W_{ele}	Electrolyte content per unit volume (kg/m^3)
W_p	Carbon content per unit volume cathode
Gree	ɛg/m^3) k symbols
α_a α_c	Anodic charge transfer coefficient
β	Cathodic charge transfer coefficient
ϵ	Bruggeman correlation coefficient
η	Surface emission rate
$k\hat{}$	Over potential (V)
κ	Reaction rate constant of the active material (m/s^2)
φ_l	Thermal conductivity (W/m–K)
φ_s	Liquid phase potential (V)
ρ	Solid phase potential (V)
σ_B	Density of the material (kg/m^3)
$\sigma_{e_{lff}}$	Stefan-Boltzmann constant (kg/s^3-K^3)
$\sigma_{e_{sff}}$	Effective ionic conductivity in the liquid phase (S/m)
σ_{tap}	Effective ionic conductivity in the solid phase (S/m)
υ_{tab}	Tab electrical conductivity (S/m)
ε_l ε_s	Tab volume (m^3)
	Volume fraction in the liquid phase
	Volume fraction in the solid phase

Oven tests at a preset temperature are typically used to assess the critical temperature that triggers TR [13] and to study the effect of the state-of-charge (SoC) on temperature [14–16]. A lower SoC leads to less reactive LIBs and longer TR incubation periods, whereas a higher ambient temperature increases the likelihood of TR. Changyong et al. [17] showed that TR is induced by the accumulation of heat energy and the rate of heat flux accumulation.

More recently, there has been a growing interest in the conditions that can trigger TR. Li et al. [18] proposed a model that predicts the behavior of LIBs under mechanical crushing and nail penetration. Simulations showed mechanical crushing damaged the separator, leading to internal short circuits. Nail penetration results in faster short circuits, which cause a rapid voltage drop and temperature rise. Kim et al. [19] proposed a model that predicts the effect of internal short circuits on temperature based on the size and quantity of lithium dendrites. Simulation predictions show that the maximum temperature increase is primarily determined by the size of the lithium dendrites, followed by the number of lithium dendrites. Liu et al.[3] found that side reactions caused by lithium plating increase the temperature of the battery during overcharging, whereas a battery with 70% state-of-health cycled at 313.15 K will experience TR due to solid-electrolyte-interface (SEI) decomposition.

The studies discussed have provided new insights into the process of TR in LIBs. Previous studies have used Newman's and Hatchard's electrochemical models to predict working voltage and thermal response during discharge and abuse tests, respectively. However, to the best of the author's knowledge, a well-established model that can predict TR during the operation of a battery is not available. To address the above-mentioned research gap, the study in this paper attempts to develop a model using a multidomain approach to predict heat generation, battery temperature, and the possibility of TR under various operating conditions.

This model estimates the heat generated by electrochemical reactions that describe kinetics, charge conservation, and mass conservation reactions within the battery's solid and electrolyte phases. When the temperature of the battery reaches a critical level, an additional heat-generating process starts. Decomposition of the SEI, anode, cathode, and electrolyte generates heat, further increasing the battery temperature. In this paper, these processes are modeled to predict whether a certain operating condition leads to TR. The model developed is verified with experiments on a 3 Ah LG HG2 NMC-811/SiC and 1.6 Ah pouch $LiFePO_4$ battery, and it is shown that the TR is well predicted. The model is valuable for designing battery pack systems that are more resilient to TR and possibly have a higher energy density. Also, this model is useful for providing early warning to passengers. We believe this study contributes to existing knowledge and can improve battery management systems for high-energy-density LIBs to prevent TR.

The rest of the paper is organized as follows: Section 2 describes the experimental setup for monitoring working voltage and surface temperature behavior under different operating conditions. Section 3 shows the description of the test battery. Section 4 introduces the electrochemical and thermal models used to predict the behavior of the battery. Section 5 discusses the tuning scheme of the model's parameters. Then, results and discussions are detailed and analyzed in Section 6. Finally, conclusions are reported in Section 7.

2. Experimental setup

An experimental setup is essential to verifying any model developed for predicting the thermal behavior of the batteries studied here. For this purpose, an experimental setup is designed to perform constant-current charging and discharging tests at various rates from 1C to 5C under controlled environmental conditions. The experimental setup used here to satisfy these requirements is presented in Fig. 1. It comprises an electronic load, a thermal chamber, a data logger system, a DC power supply, and two 3-wire RTP platinum thermistors. The electronic load and a DC power supply are used to discharge and charge the battery in galvanotactic mode. The data logger is used to monitor the working voltage and temperature variations over time. The thermal chamber is used to maintain a constant ambient temperature throughout the experiment. The 3-wire RTP platinum thermistors are tapped 0.016 m from the top and bottom of the battery under test for temperature measurement.

3. Test battery description

Two different lithium-ion batteries are tested and simulated in this study to verify the developed model. The first of the batteries is an 18650 single cell in the commercial-type 3 Ah 3.6 V LG HG2 battery displayed in Fig.2a. Its model is developed based on CT images published in [15] and shown in Fig.2b. The 3D calculation domain is reduced to a 2D cross-section perpendicular to the battery axis in this study to reduce the computational cost, as axial potential loss and active material transmission are negligible [10, 20]. The LG HG2 battery is wound with five main domains: the positive current collector (PC), the positive electrode (PE), the separator (SP), the negative electrode (NE), and the negative current collector (NC). In addition to the five main domains, the battery comprises the can (steel) and the

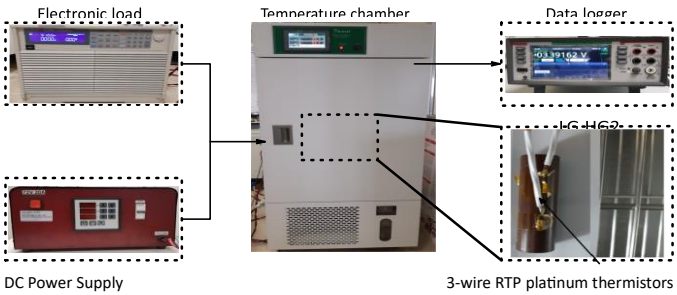

Figure 1: Experimental setup for measuring working voltage and temperature.

heat-shrink wrapping film (polyethylene terephthalate). The active material in the PE is nickel manganese cobalt (NMC-811), and in the NE it is silicon graphite (SiC). The SP, made of Celgard 2325, is a porous polymer membrane that is permeable to lithium-ions but restrains the electrons. Nguyen [21] showed that the main solvent of the LG HG2 is composed of DMC, EC, PC, and diethyl carbonate. This type of electrolyte was examined by Valøen et al. [22]. To ensure lithium-ion transfer between the electrodes, the PE, SP, and NE are immersed in a 1 M LiPF6 electrolyte in PC/EC/DMC [22]. The current collectors collect the current of the battery, which are metal foils made of aluminum (PC) and copper (NC) as seen in Fig.3. The LG HG2 has two negative tabs (one located in the innermost end and one in the outermost end of the spiral wound) in addition to one positive tab located near the middle of the spiral wound [15] as shown in Fig.2f. The PC is assumed to be welded to an aluminum tab (Fig.2c), whereas the NC is welded to a copper-nickel alloy tab (Fig.2d,e) [23].

The second test battery (pouch battery) is a commercially available 1.6 Ah 3.6 V pouch battery with outer dimensions of 0.06 m × 0.07 m × 0.003 m as seen in Fig.2g. The internal arrangement of the battery is laminated and follows the approach published in [24]. The multilayered cell is constructed with 10 PE, 10 NE, 10 SP, 6 NC, and 5 PC, as shown in Fig.2i. The active material of the PE is $LiFePO_4$, whereas it is graphite in the NE. The separator is assumed to be Celgard 2325. The electrolyte commonly used for $LiFePO_4$ batteries is R&D 281 [25] which contains 1 M dm^{-3} $LiPF_6$ in EC/EMC (3/7 V/V) with 1% VC. This type of electrolyte was investigated by A. Nyman et al. [26].

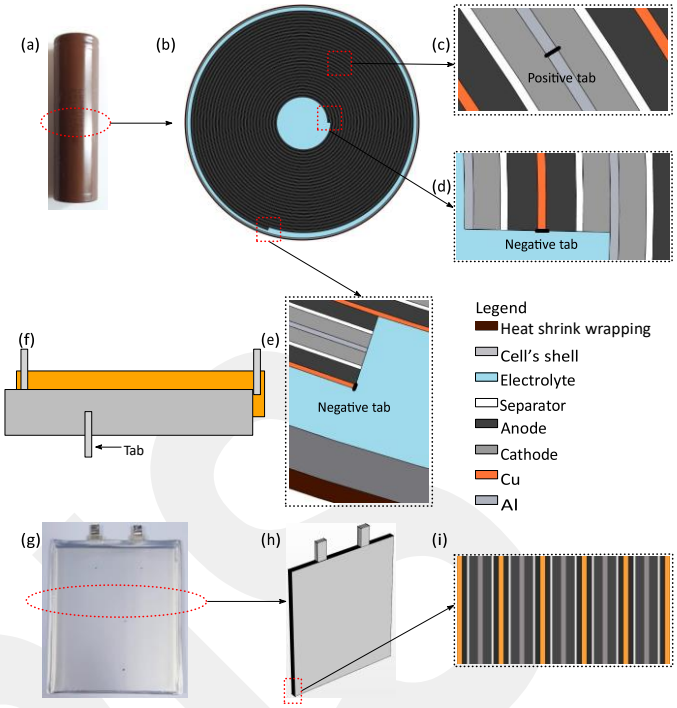

Figure 2: (a) LG HG2; (b) 2D model geometry implemented; (c) positive tab boundary; (d) inner negative tab boundary; (e) outer negative tab boundary; (f) metal foils unwounded view; (g) Second battery under test, (h) 3D equivalent geometry used, (i) Internal layout of the battery.

4. Electrochemical and thermal models

A reliable battery model is essential for predicting battery behavior under different operating conditions. This section describes the modeling procedure used in this study to predict the behavior of the test batteries. The implemented model accounts for electrochemical and thermal reactions occurring within the battery, sharing computational domains.

Newman's electrochemical model [8] describes electrochemical kinetics, charge conservation, and mass conservation reactions within the battery's solid and electrolyte phases, modeling the electrodes as porous matrices filled with spherical active particles of uniform size. Besides Newman's electrochemical reactions, an additional electrochemical process begins at a critical temperature. Hatchard's electrochemical decomposition model [27] becomes active at this temperature, accounting for the decomposition of the solid-electrolyte-interface (SEI), anode-electrolyte reaction, cathode-electrolyte reaction, and electrolyte decomposition. In this manner, it is used to predict heat generation due to decomposition reactions leading to TR. Heat generation predicted by Newman's and Hatchard's models forms the foundation for predicting the lithium-ion battery temperature response. Once the generated heat energy is estimated, heat transfer and thermal gradients within the battery can be calculated using the Bernardi's thermal model [28].

The working principle of a test battery is shown in Fig.3. Lithium ions are deintercalated from negative SiC(graphite) particles and flow to positive NMC-811($LiFePO_4$) particles through the electrolyte and separator during discharge. During discharge, the current includes electronic and ionic currents in NE and PE but only ionic current in the SP [24], as the electrolyte and separator do not conduct electrons [10, 20, 29].

The ionic current flows through the separator, enabling current transfer [29]. Lithium ions react with electrons flowing through an external circuit to intercalate into positive NMC-811($LiFePO_4$) particles. Electrochemical reactions at the electrolyte-electrode interface are expressed in table 1.

Table 1: Electrochemical reaction for both batteries during cycling

Battery	Anode	Cathode
18650	$Li_xSi \xrightarrow{\text{discharge}} Li_{x-z}Si + zLi^+ + ze^-$	$Li_{y-z}NMC_{811} + zLi^+ + ze^- \xrightarrow{\text{discharge}} Li_yNMC_{811}$
Pouch	$Li_xC_6 \xrightarrow{\text{discharge}} Li_{x-z}C_6 + zLi^+ + ze^-$	$Li_{y-z}FePO_4 + zLi^+ + ze^- \xrightarrow{\text{discharge}} Li_zFePO_4$

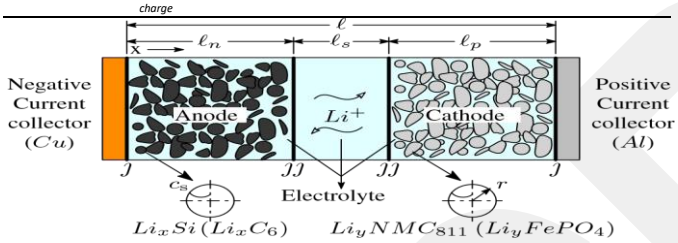

Figure 3: 2D cross-section of a test battery and its domains.

Table 2 lists the governing equations applied in each domain of the battery (Fig.2b,i) in both Newman's and Hatchard's models. The processes given in table 2 and how they generate heat are discussed in the following subsections.

Table 2: Governing equations used in each domain

Governing equation	Current collector	PE/NE	SP/Electrolyte	Can/Wrapping film
Electrochemical kinetics	-	☑	-	-
Charge conservation	☑	☑	☑	-
Mass conservation	-	☑	☑	-
Negative-solvent reaction	-	☑	-	-
Positive-solvent reaction	-	☑	-	-
SEI reaction	-	☑	-	-
Electrolyte reaction	-	☑	☑	-
Energy equation	☑	☑	☑	☑

4.1. Newman's electrochemical model

In this section, the process of heat generation over time due to activation reactions, ionic species transport, and charge transfer is predicted using Newman's electrochemical model. This model employs concentrated solution theory to account for lithium-ion transport within the electrolyte, and porous electrode theory to characterize the electrode's porous structure [8]. The process that involves heat generation requires computing the current density (j_{loc}), reaction overpotentials (η), ionic (i_l), and electronic current (i_s) in the domains displayed in Fig.3. Lithium concentration adheres to mass conservation law discussed in section 4.1.3. The lithium concentration in both phases forms the foundation for computing the exchange current density (j_0) from (2), which is then used to obtain j_{loc} from (1) at the surface of the electrode particles. The lithium concentration (c_s) in the particle grain shown in Fig.3 is calculated from (14) in the solid phase. In the electrolyte phase, the lithium concentration (c_l) is computed from (15) along the battery's thickness direction.

Charge conservation law governs the current flux within the battery, as considered in section 4.1.2. The ionic current (i_l) from (9) adheres to concentration solution theory, and it is required to determine the electrolyte phase reaction potential (φ_s). The electronic current (i_s) from (8) follows Ohm's law, and it is coupled to Faraday's law to obtain the solid phase reaction potential (φ_l). Reaction potentials in both phases are crucial for the prediction of η from (3). The experimentally determined equilibrium potential (OCV) and entropic coefficients for the LG MJ1 battery from Sturm et al. [30] are adopted in this study. The literature does not currently publish these parameters for the LG HG2 battery. However, they are expected to be similar to those of the LG MJ1 battery, since both batteries are manufactured by LG and share a similar chemistry. The OCV and entropic coefficients taken from [31] are adopted for the second battery.

Electrochemical kinetics, which couples the solid and electrolyte phases, comprises equilibrium and dynamic components. The equilibrium component (4) governs the temperature-dependent variation in the open circuit potential of the NE and PE domains. The dynamic component (1) accounts for the charge transfer chemical reaction due to a reduction and oxidation process happening during an operating condition. The Arrhenius law describes the temperature dependence of the diffusion coefficients and reaction rates of each phase. Heat generation in various battery operation stages is obtained with known (1), (3), (8), and (9). The process that contributes to heat generation is attributed to irreversible heat generation ($\dot{Q}_{irr}$) from (20), reversible heat generation ($\dot{Q}_{rev}$) from (21) following the Peltier effect, and ohmic heat generation ($\dot{Q}_{ohm}$) from (22) in each domain shown in Fig.3. The governing equations for the electrochemical kinetics are given in section 4.1.1, while the charge and mass conservation are in sections 4.1.2 and 4.1.3, respectively. Finally, heat generation due to Newman's model is addressed in section 4.1.4. The nomenclature section provides detailed definitions of all variables in the governing equations.

4.1.1. Electrochemical kinetics

Heat generation from entropy changes and activation reactions depends on both the local current density and the circuit potential of each electrode. The Butler-Volmer equation (1) predicts j_{loc} at the surface of the electrode particles, representing the rate of electric charge flow through the PE and NE. The SoC is computed as the ratio of the lithium-

ion surface concentration to the maximum solid-phase concentration.

$$j_{\mathrm{loc}} = j_0\left[\exp\left(\frac{\alpha_a F\eta}{RT}\right) - \exp\left(\frac{\alpha_c F\eta}{RT}\right)\right], \tag{1}$$

$$j_0 = F\hat{k}c_s^{\max}\sqrt{\frac{c_l}{c_l^{\mathrm{ref}}}}\sqrt{\frac{c_s^{\mathrm{surf}}}{c_s^{\max}}\left(1-\frac{c_s^{\mathrm{surf}}}{c_s^{\max}}\right)}, \tag{2}$$

$$\eta = \phi_s - \phi_l - j_{\mathrm{loc}}R_f - U_{\mathrm{eq}}, \tag{3}$$

$$U_{\mathrm{eq}} = U_{\mathrm{eq}}^{\mathrm{ref}} + \frac{dU_{\mathrm{eq}}^{\mathrm{ref}}}{dT}(T - T_{\mathrm{ref}}). \tag{4}$$

4.1.2. Charge conservation

The ohmic loss depends on the electronic and ionic currents. In the solid (NE/PE) and electrolyte phases, the electronic (i_s) and ionic (i_l) current density follows the charge conservation law,

$$\nabla \cdot i_s + \nabla \cdot i_l = 0, \tag{5}$$

$$\nabla \cdot i_s = S_a j_{\mathrm{loc}}, \tag{6}$$

$$\nabla \cdot i_l = -S_a j_{\mathrm{loc}}. \tag{7}$$

The NE, PE, and current collector domains in Fig.3 follows Ohm's law (8),

$$i_s = -\sigma_s^{\mathrm{eff}}\nabla\phi_s. \tag{8}$$

In the electrolyte phase, lithium ions move over the electrolyte through electromigration and diffusion [24]. Local ionic current density is obtained from (9) where the first and second terms are governed by Ohm's law and the ionic concentration gradient, respectively.

$$i_l = \sigma_l^{\mathrm{eff}}\nabla\phi_l + \frac{2RT\sigma_l^{\mathrm{eff}}}{F}\left(1-t_+^0\right)\left(1+\frac{d\ln f_\pm}{d\ln c_l}\right)\nabla\ln c_l. \tag{9}$$

The boundary JJ in Fig.3 is insulated from electronic current in the solid phase and has continuous ionic current and lithium-ion flux in the electrolyte phase, while the boundary J is insulated from the ionic current. The positive tab (Fig.2c) current equals the operating current (I_{app}), while the negative tabs (Fig.2d,e) are grounded. These boundary conditions are expressed as follows:

$$-\sigma_s^{\mathrm{eff}}\nabla\phi_s\Big|_{x=\ell_n\ \&\ x=\ell_n+\ell_s} = 0, \tag{10}$$

$$-\sigma_l^{\mathrm{eff}}\nabla\phi_l\Big|_{\ell_n^-/\ell_n^+} = -\sigma_l^{\mathrm{eff}}\nabla\phi_l\Big|_{(\ell_n+\ell_s)^-/(\ell_n+\ell_s)^+}, \tag{11}$$

$$\nabla\phi_l\Big|_{x=0\ \&\ x=\ell} = \nabla\phi_s\Big|_{x=\ell} = 0, \tag{12}$$

$$-\sigma_s^{\mathrm{eff}}\nabla\phi_s\Big|_{positive\ tab} = I_{\mathrm{app}}. \tag{13}$$

4.1.3. Mass conservation

Porous electrodes consist of individual spherical particles surrounded by electrolyte allowing interaction between particles as seen in Fig.3. Lithium-ion concentrations in the solid particles of the electrodes follow Fick's second law in spherical coordinates, describing the diffusion of lithium-ions in the solid phase,

$$\frac{\partial c_s}{\partial t} = \frac{1}{r^2}\frac{\partial}{\partial r}\left(r^2 D_s\frac{\partial c_s}{\partial r}\right). \tag{14}$$

In the liquid phase, the molar flux of lithium ions accounts for Fick's law and electromigration,

$$\varepsilon_l\frac{\partial c_l}{\partial t} + \nabla\cdot\left[-D_l^{\mathrm{eff}}\nabla c_l + \frac{i_l\left(1-t_+^0\right)}{F}\right] = \frac{S_a j_{\mathrm{loc}}}{F}. \tag{15}$$

Lithium-ion diffusion flux in the center of the particle grains in Fig.3 is zero due to symmetry but follows Fick's first law on the surface to relate the grain-wall lithium-ion flux to the lithium-ion diffusion rate into the NE/PE surface. Lithium-ion transport is confined to the batteries domains, leading to zero mass flux at the boundary J in Fig.3. With this considerations, the boundary conditions for lithium-ion concentrations in solid particles and mass transport of lithium-ions are as follows:

$$\frac{\partial c_s}{\partial r}\Big|_{r=0} = 0, \tag{16}$$

$$-D_s\frac{\partial c_s}{\partial r}\Big|_{r=R_p} = \frac{j_{\mathrm{loc}}}{S_a F}, \tag{17}$$

$$-\sigma_l^{\mathrm{eff}}\nabla c_l\Big|_{x=0\ \&\ x=\ell} = 0, \tag{18}$$

$$-\nabla c_l\Big|_{\ell_n^-/\ell_n^+} = -\nabla c_l\Big|_{(\ell_n+\ell_s)^-/(\ell_n+\ell_s)^+}. \tag{19}$$

4.1.4. Heat generation due to Newman's model

In the solution of the problem, determining j_{loc}, η, i_l, i_s, φ_l, φ_s in each simulation step is necessary before estimating heat generation from activation reactions, ionic species transport, and electronic charge transfer as follows:

$$\dot{Q}_{\mathrm{irr}} = S_a j_{\mathrm{loc}}\eta, \tag{20}$$

$$\dot{Q}_{\mathrm{rev}} = S_a j_{\mathrm{loc}} T\frac{\partial U_{\mathrm{eq}}}{\partial T}, \tag{21}$$

$$\dot{Q}_{\mathrm{ohm}} = -i_s\nabla\phi_s - i_l\nabla\phi_l. \tag{22}$$

A new electrochemical process that generates further heat starts upon reaching a critical temperature. This process is explained in section 4.2.

4.2. Hatchard's electrochemical decomposition model

Hatchard's electrochemical decomposition model predicts heat and mass flow generation once a critical temperature is reached. The model describes the time-dependent evolution of the concentration reaction species in exothermic decomposition reactions [32]. It expresses the thermochemical kinetics and temperature-dependent material transport parameters of the domain's material through the Arrhenius law.

Thermal runaway is a multistep process characterized by a series of exothermic reactions triggered by battery material decomposition at elevated temperatures, leading to a rapid rise in battery temperature [32]. Thermal runaway comprises four consecutive stages initiated by the onset of exothermic decomposition reactions. The initial stage of TR shows heat generation at a rate of 0.003 K/min. Stage 2 characterizes self-heating at a rate greater than 0.02 K/min, leading to the beginning of SEI decomposition. Anode-electrolyte decomposition occurs as the decomposition progresses. Stage 3 is characterized by separator decomposition and internal short circuits due to direct contact between electrodes, while stage 4 exhibits a sudden temperature rise [33]. The onset temperature of each decomposition is determined using the heat-wait-seek method by monitoring the self-heating surface temperature rate during the seek phase [13]. Each of the above-mentioned decomposition reactions starts once a critical surface temperature is reached. Usually, the critical temperature for the SEI starts between 333.15393.15 K, for the negative-solvent reaction between 393.15-
523.15 K, for the positive-solvent reaction around 403.15 K443.15 K, and finally, the electrolyte usually decomposes at temperatures near 473.15 K [21, 34]. In the following sections, the heat generation process at various stages of battery temperature is discussed. The nomenclature section provides detailed definitions of all variables in the governing equations, whereas an in-depth interpretation of each decomposition reaction is given in [27, 35].

4.2.1. SEI decomposition reaction

The ionically conducting SEI layer protects the particle grains in the solid phase from direct reaction with the electrolyte. This layer becomes unstable and starts to exothermically decompose after 333.15-393.15 K [21, 35, 36].The solutions of (23)-(24) yield the reaction rate R_{sei}, which enables the prediction of heat generation $\dot{Q}_{sei}$ due to the decomposition of the SEI from (34).

$$R_{sei} = A_{sei} \exp\left(-\frac{Ea_{sei}}{k_B T}\right) c_{sei}^{m_{sei}}, \tag{23}$$

$$\frac{dc_{sei}}{dt} = -R_{sei}. \tag{24}$$

The next reaction in the sequence involves the reaction between intercalated lithium in NE and electrolyte, as described in section 4.2.2.

4.2.2. Negative decomposition reaction

The decomposition between the electrolyte and the particle grains of the NE leads to the growth of the SEI layer and a change in the amount of intercalated lithium in the NE due to aging. In this study, it is assumed that the behavior of the cell during TR is not impacted by those changes, as in [21]. With this assumption the decomposition reaction in negative electrode can be expresses as follows:

$$R_{ne} = A_{ne} \exp\left(-\frac{t_{sei}}{t_{sei,ref}}\right) c_{ne}^{m_{ne}} \exp\left(-\frac{Ea_{ne}}{k_B T}\right), \tag{25}$$

$$\frac{dc_{ne}}{dt} = -R_{ne}, \tag{26}$$

$$\frac{dt_{sei}}{dt} = R_{ne}. \tag{27}$$

Solving (25)-(27) yields the reaction rate R_{ne} enabling the estimation of heat generation $\dot{Q}_{ne}$ due to anode decomposition from (35). Anode decomposition raises the battery temperature further, leading to the PE decomposition reaction described in section 4.2.3.

4.2.3. Positive decomposition reaction

The particle grains in the PE react exothermically with the electrolyte in their oxidized state, leading to the production of oxygen [21]. Equations (28)-(29) are used to predict the cathode decomposition reaction rate R_{pe} due to this process to determine the cathode decomposition heat generation $\dot{Q}_{ne}$ from
(36).

$$R_{pe} = A_{pe} \alpha^{m_{pe1}} (1-\alpha)^{m_{pe2}} \exp\left(-\frac{Ea_{pe}}{k_B T}\right), \tag{28}$$

$$\frac{d\alpha}{dt} = R_{pe}. \tag{29}$$

Electrolyte decomposition typically begins at approximately 473.15 K [21, 34]. This is discussed in section 4.2.4.

4.2.4. Electrolyte decomposition reaction

The electrolyte salt $LiPF_6$ is unstable at high temperatures and oxidizes upon contact with oxygen. The electrolyte decomposition reaction reduces the electrolyte amount, resulting in a drop in the dimensionless variable c_{ele}. The total heat generation due to this reaction depends on the total amount of electrolyte [35]. Upon computing (30)-(31), the reaction rate R_{ele} is obtained, and hence the heat generation $\dot{Q}_{ele}$ is predicted from (37).

$$R_{ele} = A_{ele} \exp\left(-\frac{Ea_{ele}}{RT}\right) c_e^{m_{ele}}, \tag{30}$$

$$\frac{dc_{ele}}{dt} = -R_{ele}. \tag{31}$$

Heat generation from material decomposition leads to high temperatures, causing the melting of the separator domain seen in Fig.3. Internal short circuits occur once the separator melts, as discussed in section 4.2.5.

4.2.5. Internal short circuit reaction

Melting of the separator at high temperatures yields direct contact between the NE and PE domains, producing internal short circuits (ISC) and a voltage drop. This process quickly releases energy internally with a non-Arrhenius rate, which

depends on the battery's SoC [14–16, 37, 38], voltage, and battery's capacity. Feng et al. [39] modeled voltage drop due to an internal short circuit (ISC) with an electric circuit that accounts for electrode voltage drop, ohmic potential loss, and entopic changes due to high temperatures. Nguyen [21] studied the voltage drop due to an ISC and showed that it can be modeled through a second-order resistor-capacitor equivalent circuit model. Coman et al. [38] stated that an Arrhenius formulation can be used to describe the electrochemical reaction in which the SoC changes as a function of time. The internal short circuit reaction in this study is computed as follows [21, 38, 40, 41]:

$$H_{\text{isc}} = -3600 \cdot V_{\text{cell}} \cdot C_{\text{cell}}, \tag{32}$$

$$\frac{dSoC}{dt} = A_{\text{isc}} SoC \exp\left(-\frac{Ea_{\text{isc}}}{k_B T}\right). \tag{33}$$

The solution of (32)-(33) yields the reaction rate H_{isc} enabling the calculation of heat generation $\dot{Q}_{\text{isc}}$ due to this process from (38).

4.2.6. Heat generation due to Hatchard's model

Once the critical temperature is reached, heat generation follows. The decomposition reactions above explained are solved in each simulation step once the critical temperature is reached. Heat generation from exothermic decomposition reactions of the various battery materials is calculated once the reaction rate is known as follows:

$$\dot{Q}_{\text{sei}} = H_{\text{sei}} W_c R_{\text{sei}} \tag{34}$$

$$\dot{Q}_{\text{ne}} = H_{\text{ne}} W_c R_{\text{ne}}, \tag{35}$$

$$\dot{Q}_{\text{pe}} = H_{\text{pe}} W_p R_{\text{pe}}, \tag{36}$$

$$\dot{Q}_{\text{ele}} = H_{\text{ele}} W_{\text{ele}} R_{\text{ele}}, \tag{37}$$

$$\dot{Q}_{\text{isc}} = H_{\text{isc}} A_{\text{isc}} \exp\left(-\frac{Ea_{\text{isc}}}{k_B T}\right) V_{\text{cell}}. \tag{38}$$

The temperature field in the LIB is determined once heat generation is predicted. After computing heat generation, temperature is estimated using the model explained in the next subsection.

4.3. Bernardi's thermal model

The process which generates heat are discussed in the previous sections. Once the heat energy and initial temperature of the battery are known, its temperature over a time interval can be calculated. Once the heat generated in each domain is known, the spatial and temporal temperature gradients in each domain of the battery are determined by Bernardi's thermal model from

(39). This approach takes into account Fourier's law, Stefan-Boltzmann's law, and Newton's law of cooling. The nomenclature section provides detailed definitions of all variables in the governing equations.

$$\rho C_p \frac{\partial T}{\partial t} = \kappa \nabla^2 T + \dot{Q}_{\text{tot,N}} + \dot{Q}_{\text{tot,H}} + \dot{Q}_{\text{tot,tab}}. \tag{39}$$

The total heat generation due to Newman's electrochemical model is defined as the summation of the heat generation from (20)-(22) and it is denoted by $\dot{Q}_{\text{tot,N}}$. Likewise, the total heat generation due to Hatchard's decomposition electrochemical model takes the form $\dot{Q}_{\text{tot,H}}$ where each decomposition reaction is calculated according to (34)-(38).

$$\dot{Q}_{\text{tot,N}} = \dot{Q}_{\text{irr}} + \dot{Q}_{\text{rev}} + \dot{Q}_{\text{ohm}}, \tag{40}$$

$$\dot{Q}_{\text{tot,H}} = \dot{Q}_{\text{sei}} + \dot{Q}_{\text{ne}} + \dot{Q}_{\text{pe}} + \dot{Q}_{\text{ele}} + \dot{Q}_{\text{isc}}. \tag{41}$$

The ohmic heat loss on each tab of Fig.2f follows Joule's law and is added analytically to (39). The summation of total heat loss on tabs from (42) is defined as $\dot{Q}_{\text{tot,tab}}$.

$$(\varsigma = \text{NC}, \text{PC}) : \dot{Q}^{\varsigma}_{\text{tab}} = \frac{L^{\varsigma}}{\sigma^{\varsigma}_{\text{tap}} A^{\varsigma}_{\perp} v^{\varsigma}_{\text{tab}}} I^2_{\text{app}} \tag{42}$$

Heat dissipation due to Stefan-Boltzmann law and Newton's law of cooling is applied on the battery's surface as a boundary condition, whereas continuity of heat flux is imposed between domains (ȷ/ȷȷ in Fig.3)

$$-\kappa \nabla T = h(T - T_\infty) + \epsilon \sigma_B \left(T^4 - T_\infty{}^4\right), \quad (43)$$

where T_∞ is an infinite boundary condition representing the ambient temperature.

4.4. Coupling between models

The coupling between the electrochemical and thermal models is attained through local temperature, as shown in Fig. 4. The sum of the total heat generated by (40) and (41) is fed to (39) to predict the LIB's temperature field.

4.5. Meshing of the model

Accuracy of numerical calculations depend on meshing, model parameters, and the solver used to solve the governing equations of the model. A swept-method approach is used to build a quad mesh by finely meshing the PC/NC, NE/PE, SP,

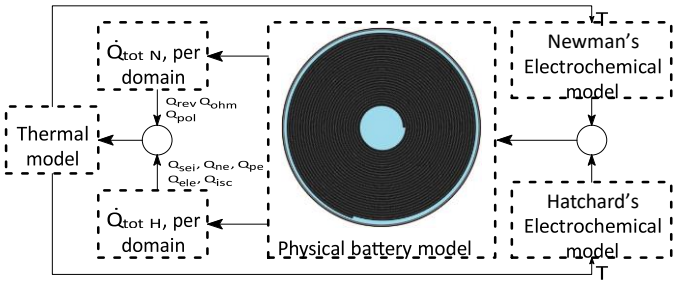

Figure 4: Coupling scheme.

heat-shrink wrapping, and battery's shell domain, as seen in Fig.2c,d,e. A free triangular mesh is used for the remaining

domains. A mesh independence test was performed to ensure that predictions of voltage and surface temperature are not sensitive to the mesh size. The mesh was refined until voltage and surface temperature predictions showed no significant changes. Three mesh grid sizes: coarse, normal, and fine, are used to perform the mesh independence test. To verify that the meshing is acceptable, a constant discharge current test is performed on the test batteries. The variation of battery surface temperature over time is recorded. In this test, the battery is discharged at 4C at an ambient temperature of 298.15 K until the cut-off voltage of 2.5 V is reached. The same experiment is performed via simulation using the three meshes created for the battery model. The prediction of surface temperature for both batteries is compared to the measurement in Table 3 for the LG HG2. The mean absolute percentage error (MAPE) for each case is presented in the same table.

Table 3: Grid sizes, computational times, and errors

Grid size	Mesh vertices		Computational time (s)		MAPE (%)	
	LG	Pouch	LG	Pouch	LG	Pouch
Coarse	27989		858		8.64	
Normal	137966		3153		6.40	
Fine	219017		8091		6.12	

Simulation work was executed on an i7–11700 @ 4.34 GHz and 16 GB Ram

From this table, a marginal improvement in the accuracy of the model is obtained when using a fine mesh size compared to a normal mesh size. A normal mesh grid size is sufficient to obtain accurate predictions in a short time. The selected mesh used in this study for the first battery is presented in Fig.5a.

It is made up of 2830 triangular elements, 136488 quadrilateral elements, 26 vertex elements, and 27704 edge elements, with maximum and minimum element sizes of 2.4×10^{-7} m and 1.22×10^{-3} m, respectively. Skewness is used to assess the mesh quality, with 1 being considered optimal. In this study, the skewness is 0.9765. The same test analysis was performed on the second battery. The resulting mesh for the second battery in Fig.5b comprises a total of 702 vertex elements, 121000 hexahedral elements, and 8228 edge elements, with maximum and minimum element sizes of 3.2×10^{-3} m and 0.8×10^{-3} m, respectively.

4.6. Numerical solution of the problem

The electrochemical-thermal coupled equations, with the corresponding boundary conditions, is solved using a finite element (FE) approach, employing commercial software. The

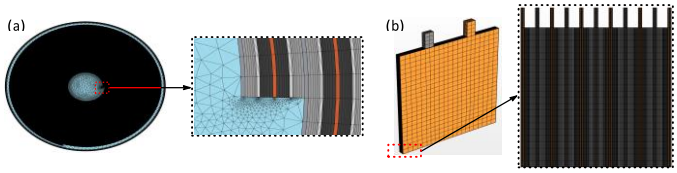

Figure 5: Resulting model's mesh. a) LG HG2 battery, b) Pouch battery; axial dimension is magnified to make meshing visible

model's outputs are the battery's working voltage, heat generation, and temperature fields of each mesh. At each time step (5 s), the heat generation is first calculated based on the current operating condition and is then considered as a local heat source to obtain temperature distribution in the battery. Local temperature is then used to update the physiochemical variables that are temperature-dependent on each model. In the solution of the problem, the parallel direct sparse solver is adopted. Convergence is assumed when the change in the solution from one iteration to the next is lower than a relative tolerance error of 10^{-4}.

5. *Tuning of model parameters*

To assure the accuracy of the model, tuning the electrochemical-thermal model parameters for the LG HG2 and pouch battery is essential. Accurate models are essential for ensuring lithium-ion battery predictions under various operating conditions. Comparing tuned model predictions with experimental data ensures accuracy and reliability. Figure 6 presents the tuning scheme used for the electrochemical and thermal models. Parameter tuning is conducted for Newman's and Bernardi's models. Hatchard's electrochemical decomposition model parameters for the LG HG2 battery are given in [21], whereas they are taken from [42] for the second battery.

The Newman's electrochemical parameters to be adjusted are the active material volume fraction in the solid phase (ε_s), maximum lithium-ion concentrations (c^{max}_s), diffusion coefficients (D^{ref}_s), reaction rates ($k^{\wedge ref}$), cathode's Bruggeman correlation (β), and SoC stoichiometry coefficient (100% and 0% SoC). These are the most sensitive parameters reported in the literature [16]. The heat transfer coefficient is the only parameter adjusted in Bernardi's thermal model.

To tune the parameters of the implemented model for predictions of voltage and temperature rise, a set of experiments were performed on the test batteries. The experimental test consisted

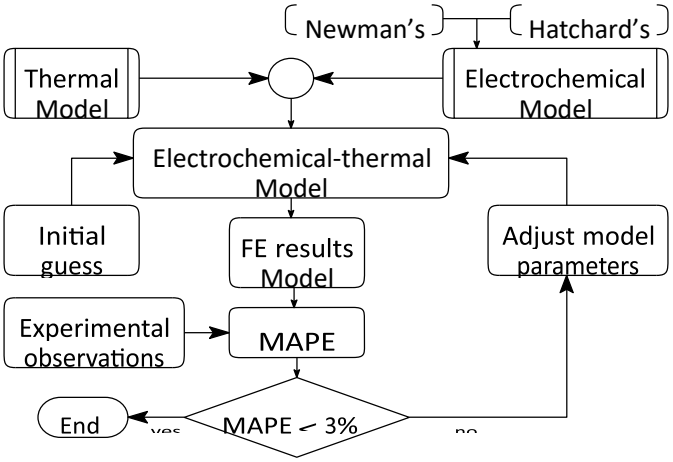

Figure 6: Parametrization scheme used in this study.

of discharging the battery at different current levels and ambient and battery temperatures of 298.15 K using the setup described in Section 2. Each test ends when the voltage criteria limit of 2.5 V is reached. A 100% SoC battery is placed in the thermal chamber for one hour prior to the experiment and then allowed to relax for two hours after each experiment. The battery's working voltage is measured at its terminals, and the surface temperature is the average of the thermistor measurements. Simulations of the same experiments are then performed, and the selected parameters are iteratively tuned in the simulation until the MAPE between measurement and prediction is less than 3%. Calibration requires a set of initial parameters, used only for the first iteration. Next iterations first adjust stoichiometry parameters at 100% SoC until the predicted initial voltage agrees with measurement. The maximum lithium ion concentrations, diffusion coefficients, and reaction rates are reported in the literature to affect discharging time [25]. These parameter sets are adjusted next. Adjusting the active material volume fractions and heat transfer coefficients is the final step. The parameters of the second test battery (pouch battery is tuned in the same manner.

6. Verification of tuned parameters

Figure 7 compares the model's prediction (after parameters' tuning) to experimental measurements under the conditions stated before for the first battery for current levels of 1C-5C.

The results show that the predictions match the experiments well. The MAPE between the predicted voltage and measurement at different C-rates is 0.96, 0.79, 0.99, 0.92, and 1.22 percent for 1C-5C, respectively. The MAPE of the temperature for the same C-rates is 0.24, 0.29, 0.36, 0.37, and 0.77, percent respectively. The error between predicted and measured temperatures increases with increasing C-rate, from 1C to 5C. The highest measured surface temperature rise was observed at a discharge rate of 5C as shown in Fig. 7b,

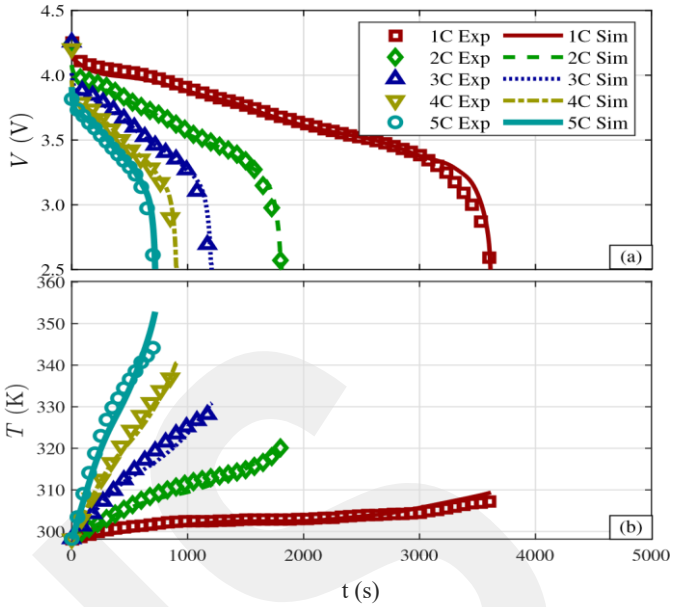

Figure 7: Measurement and prediction results of first battery for temperature and voltage variations over time. Discharge current: 1C-5C, Ambient temperature: 298.15 K.

with a temperature increase from 298.15 K to 344.23 K. when compared with measurements the absolute error is only 2.5%.

Similar experiments are performed on the second test battery. However, a full parameter set for the LG HG2 is not available in the literature. The author's of this paper parameterize this battery and tuned the parameters using the approach presented in section 5. Table 4 presents the complete set of electrochemical and thermal model parameters of the pouch test battery used in the charging discharging test simulations.

Figure 8 shows the predicted voltage and temperature of the second test battery (pouch battery) after parameter tuning for discharge rates from 1C to 4C in Fig.8. Predictions again agree well with the experiments, as shown by the results in this figure. The MAPE between the predicted voltage and measurement at different Crates is calculated as 0.74, 1.1, 1.1, and 1.2 percent for 1C-4C, respectively. The MAPE for the predicted and measured temperatures for the same C-rates is computed as 2.6, 1.4, 2.6, and 2.2 percent, respectively. The maximum surface measured temperature rise in Fig.8b was observed at a 4C discharge rate, with a 29.37 K increase (from 298.15 K to 327.52 K). The highest absolute error between the measurements and predictions occur at 4C and is only 3.2%.

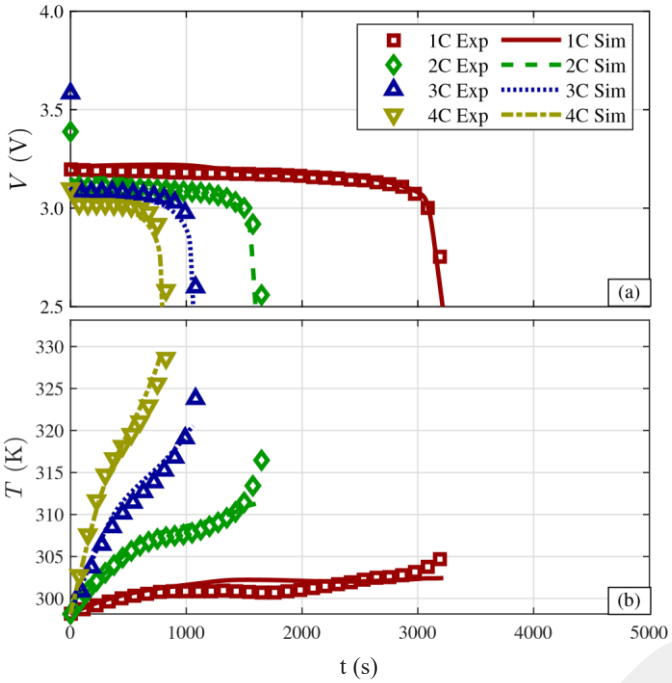

Figure 8: Comparison between experimental data and simulation results of second battery for surface temperature and working voltage variations against time.

Discharge current: 1C to 5C, Ambient temperature of 298.15 K.

Table 4: Electrochemical and thermal model parameters used in study

Parameter	NC	NE	SP	PE	PC
3 Ah 3.6 V LG HG2 battery					
Thickness (μm)	14 [I]	50 [I]	12 [I]	45 [I]	15 [I]
R_p (μm)	–	6.96 [†,D50]	–	4.98 [†,D50]	–
ϵ_s (%)	–	71 [‡]	–	80.8 [‡]	–
ϵ_l (%)	–	25 [†]	0.45 [II]	17.2 [†]	–
Inactive fraction (%)	–	4 [†]	–	2 [†]	–
U_{eq}^{ref} (V)	–	II	–	II	–
dU_{eq}/dT (mV/K)	–	II	–	II	–
c_s^{max} (mol/m^3)	–	35115 [‡]	–	41375 [‡]	–
$c_s^{initial}$ (mol/m^3)	–	28627 [‡]	–	8500.2 [‡]	–
D_s^{ref} (m^2/s)	–	$4.56 \cdot 10^{-14}$ [‡,§]	–	$3.35 \cdot 10^{-13}$ [‡,§]	–
E_D (J/mol)	–	42770 [III]	–	18550 [III]	–
k^{ref} (m/s)	–	$3.40 \cdot 10^{-10}$ [‡,§]	–	$2.27 \cdot 10^{-9}$ [‡,§]	–
E_k (J/mol)	–	35000 [III]	–	17800 [III]	–
σ_s (S/m)	II	215 [III]	–	0.18 [II,III]	II
R_f (Ωm)	–	0.0035 [II]	–	0 [II]	–
α_{sc}	–	0.5 [IV]	–	0.5 [IV]	–
β	–	1.5	1.5	1.85 [‡,*]	–
ρ (kg/m^3)	8950 [II]	2242 [IV]	1009 [II,III]	4870 [II]	2710 [II]
C_p (J/kg–K)	385 [II,III]	1437.4 [III]	1978.2 [II,III]	1269.21 [III]	903 [II,III]
κ (W/m–K)	398 [II,III]	1.04 [II,III]	0.334 [II,III]	1.58 [II,III]	238 [II,III]
h (W/m^2–K)			9 [‡]		
ϵ			0.2 [V]		
T_{amb} (K)			298.15		
[†] measured, [‡] estimated, [*] D_s, σ_1, and σ_2, [§] Arrhenius law					
[I] Ref. [22], [II] Ref. [24], [III] Ref. [21], [IV] Ref. [77], [V] Ref. [43].					
1.6 Ah 3.6 V pouch battery					
Thickness (μm)	70 [I]	72 [I]	30 [I]	120 [I]	75 [I]
R_p (μm)	–	14.75 [D50]	–	1.15 [D50]	–
ϵ_s (%)	–	56	–	43.5	–
ϵ_l (%)	–	44 [†]	0.4	50.5 [†]	–
Inactive fraction (%)	–	0 [†]	–	6 [†]	–
U_{eq}^{ref} (V)	–	I	–	I	–
dU_{eq}/dT (mV/K)	–	I	–	I	–
c_s^{max} (mol/m^3)	–	48691 [‡]	–	27946 [‡]	–
$c_s^{initial}$ (mol/m^3)	–	48690 [‡]	–	691.54 [‡]	–
D_s^{ref} (m^2/s)	–	$7.12 \cdot 10^{-14}$ [‡,§]	–	$2.05 \cdot 10^{-13}$ [‡,§]	–
E_D (J/mol)	–	4000	–	20000	–
k^{ref} (m/s)	–	$1.01 \cdot 10^{-11}$ [‡,§]	–	$3.02 \cdot 10^{-11}$ [‡,§]	–
E_k (J/mol)	–	4000 [I]	–	4000 [I]	–
σ_s (S/m)	$6 \cdot 10^7$	100	–	11.8	$3.77 \cdot 10^7$
R_f (Ωm)	–	0	–	0	–
α_{sc}	–	0.5	–	0.5	–
β	–		1.5		–
ρ (kg/m^3)	8900	2660	1009	1500	2700
C_p (J/kg–K)	385	1437.4	1978	1260.2	903
$\kappa_\perp$ (W/m–K)	398	1.06	0.334	1.79	238
$\kappa_\angle$ (W/m–K)	398	31	0.334	23	238
h (W/m^2–K)			5 [‡]		
T_{amb} (K)			298.15		
[†] measured, [‡] estimated, [*] D_s, σ_1, and σ_2, [§] Arrhenius law					
Unless otherwise stated, properties are taken form Ref. [9], [I] Ref. [41].					

7. Experiments to verify Newman's electrochemical model

To verify Newman's model a cyclic charge-discharge cycle test is performed on both batteries. Voltage and temperature predictions from these tests are presented and compared to measurements in this section. Hatchart's model developed for the test batteries is studied in section 6.2 on LG HG2 battery.

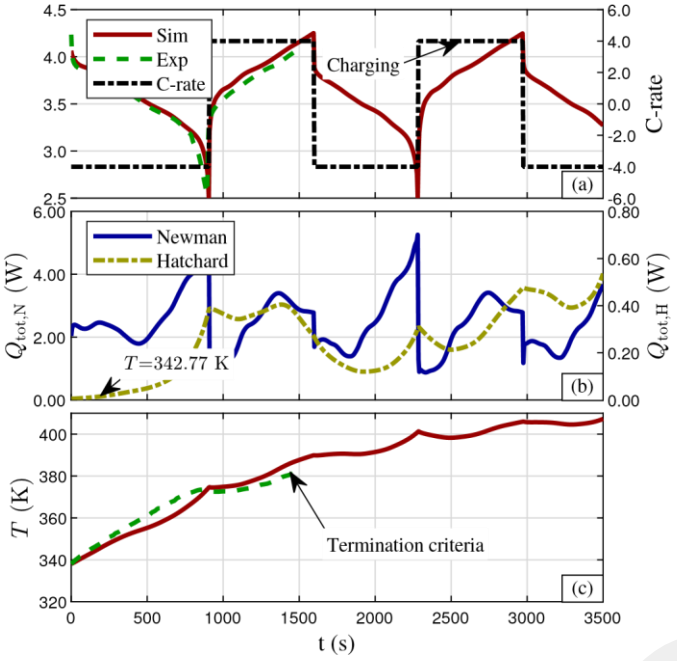

Figure 9: Measurement and predictions comparison for the LG HG2 along with heat generation prediction over time for a cyclic charge-discharge cycle. Current rate: 4C, Ambient temperature: 338.155 K. a) Voltage, b) het generation, c) surface temperature.

The experiments to verify Newman's model involve cyclic charging and discharging of the test battery at 4C using the test setup in section 2. In these tests, discharge-charge cycles were conducted for an elapsed time of 3500 s. Each cycle consists of discharging to 2.5 V, followed by galvanostatic charging to a voltage level of 4.25 V for the LG HG2 and 3.8 V for the pouch (second) battery. To avoid TR and to prevent further degradation of the LIBs, the experimental termination temperature criteria for the first and second batteries were 383.15 K and 379.15 K, respectively.

Figure 9a,c compares working voltage and surface temperature predictions to measurements for the LG HG2 battery under the stated conditions.

The predicted voltage and temperature variations over time are in good agreement with the measurements, as shown in Fig.9a,c. The predicted voltage and temperature MAPE are computed as 2.08 and 1.13 percentage, respectively. In the experiment, the termination criterion of 383.15 K was reached at t=1510 s, while the predicted surface temperature at that time was 387.92 K. When the predicted cut-off upper limit at t = 1510 s is compared to the measurement of 4.1 V, an absolute error of 2.4% is obtained. The maximum predicted temperature was 409.14 K in Fig. 9c at the end of the simulation. The average temperature rate measured in Fig. 9c from 369.15 K to 379.15 K is 1.17 K/min, while the predicted temperature rate for the same range is 1.45 K/min.

From Fig 9b, the contribution to heat generated by the battery from Newman process and from Hatchard process can be traced. It can be observed from the figure that Newman process contribution to loss ($\dot{Q}_{tot,N}$) is 7 times greater at these low temperatures than Hatchard process contribution. Hatchard process contribution oscillates around a mean value over the time period of test. Furthermore, near 0% SoC a sharp increase in the loss can be observed in Fig. 9b and loss increases with SOC as observed by Ziat et al. [12].

From Fig. 9 the heat generation due to Hatchard's model ($\dot{Q}_{tot,H}$) is observed to start at 342.77 K. The loss $\dot{Q}_{tot,H}$ increases from 0.01 W at T = 342.77 K to 0.53 W at the end of the simulation, indicating a 5200% increase.

The same test is done on the pouch battery (second) and its results are plotted in Fig.10a,c and compared with the result of model prediction for the same conditions.. The predicted voltage and temperature MAPE are computed as 1.88 and 4.45 percent, respectively. This level of MAPE indicates that In the model of the battery is accurate in prediction of voltage and temperature of the battery.

The experiment on the pouch battery is terminated at 381.28 K (106 °C) at t = 1320 s. The rate at which the surface temperature of the battery rises from 369.15 K to 379.15 K is measured as 1.58 K/min, whereas the predicted rate is 1.98 K/min, as seen in Fig.10c which is acceptably accurate.

Heat generation from Newman's and Hatchard process is presented in Fig.10b for the pouch test battery. From Fig.10b, it is observed that $Q_{tot,N}$ (Newmans) is the primary heat source, where its contribution increases rapidly towards the end of charging. Heat contribution due to $Q_{tot,N}$ agrees with the findings in [44] for a similar $LiFePO_4$ battery showing a rapid increase towards the end of the discharge. Heat generation due to $Q_{tot,H}$ (Hatchard) is observed to start after 363.15 K, which is in line with the range of temperatures (323.15-393.15 K) at which the SEI starts to generate heat [33]. The loss predicted by $Q_{tot,H}$ increased from 0.001 W at the beginning of the first charging cycle to 0.022 W at the end of the simulation, indicating a 2200% increase.

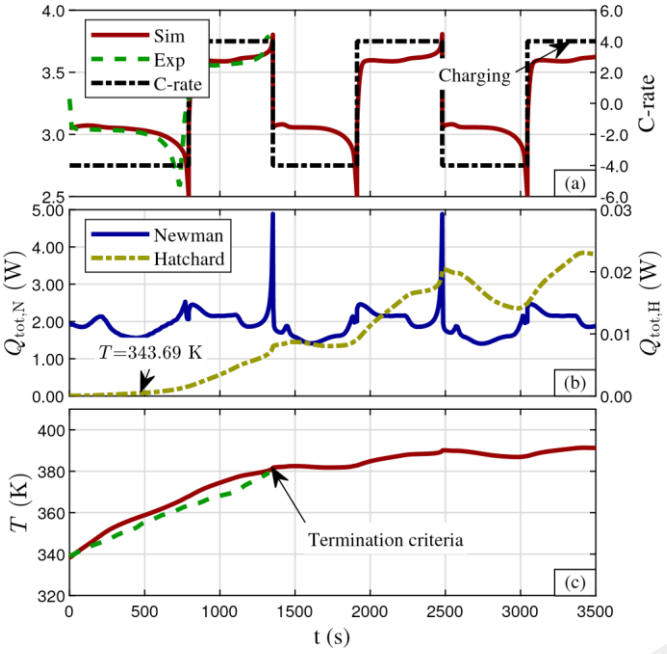

Figure 10: Measurement and predictions comparison for the pouch battery along with heat generation prediction over time for a cyclic charge-discharge cycle. Current rate: 4C, ambient temperature: 338.15 K. a) Voltage, b) het generation, c) surface temperature.

8. Experiments to verify Hatchard's electrochemical model

Experiments are needed on the test battery exceeding the critical temperature to assess the accuracy of the developed model for predicting battery temperature after the critical temperature, where Hatchard's model heat contribution is significant. Our test facility is unsafe for such temperatures; therefore, experimental results presented in [21] for a similar battery (LG HG2) are used.]. In [21} the battery is placed in an owen and the battery temperature is increased until thermal runaway occurs. determined the critical temperature of TR for the LG HG2 at a temperature rate of 48 K/min.

Before simulating the experiment reported in (Nyguen) [21], the heat transfer coefficient of the battery model is calibrated as proposed in this paper.

Next, as in Nyguen's experiment: The battery is assumed to be fully charged and disconnected from the charger. The LIB is heated by increasing the ambient temperature of the battery in the simulation is increased at a rate of 5° K/min until thermal runaway occurs.

Figure 11 compares the measured surface temperature of the battery in Nguyen's measurement the predicted results from the simulation using the model developed by the authors. Tit can be observed from the figure that the simulation predicts the measurement results with excellent accuracy. The measured critical temperature is 454.65 K; the model here predicts 452.69 K. The maximum temperature is measured as 996.15 K the model predicts 998.74K.

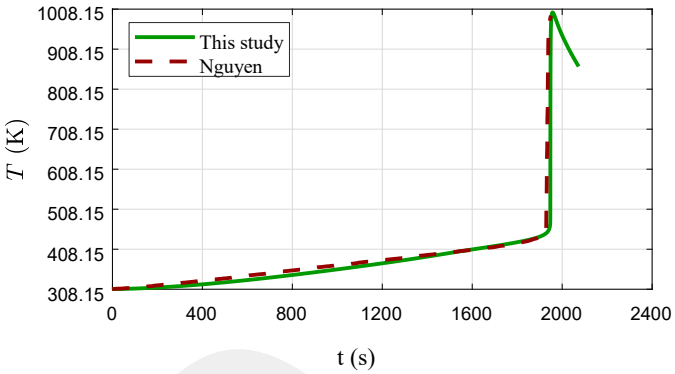

Figure 11: Surface temperature predictions from an oven test over time compared to Nguyen's results. Maximum oven temperature: 473.15 K.

The ability of the developed coupled model to predict TR in a high C-rate **discharge-charge cycle is demonstrated in the following section for both batteries.**

9. Thermal runaway prediction using the coupled model

The experimental results presented in sections 7 and 8 illustrate that the coupled model developed for predicting Lilon battery behavior (temperature, voltage ……etc) up to TR is accurate and can mimic the behavior well. Futher tests are performed on the two test batteries at high C-rate discharge-charge cycles in this section. The tests are terminated before the batteries reach TR, for safety reasons.

High operating currents increase heat generation leading to rapid temperature rise. To observe the prediction of TR in simulation, the LG HG2 is discharge-charged at 6C at an ambient temperature of 303.15 K, the average temperature in Ankara/Turkiye during summer [45]. The¨ model's initial temperature is assumed to be 338.15 K, representing a condition in which the EV has operated for a long time. The battery is cycled in simulation between 2.5 V and 4.25 V until TR is observed. The variation of thermophysical and physiochemical properties after TR is neglected.

Simulation predictions against the time of the LG HG2 for surface temperature, heat generation, and voltage are shown in Fig.12. The temperature prediction displayed in Fig.12c shows a temperature rise from 303.15 K to its maximum of 816.77 K in 1485 s. Willstrand et al. [46] argued that SoC strongly influences TR behavior, including gas volume, production rate, composition, mass loss, onset, and maximum temperature. The authors found that the maximum battery surface temperature increased by approximately 90°C per 25% increase in SoC. The SoC before the sudden temperature rise in Fig.12c was 18%. The lower SoC resulted in a lower maximum surface temperature in Fig.12c when compared to Fig.11 at 100% SoC, consistent with the literature [14–16, 21, 46].

Inspired by [2], the characteristic temperatures of TR comprise three crucial thresholds (T1-T3). T1 occurs at a heat

rate greater than 0.02 K/min. T2 represents the sudden acceleration of the temperature rate and defines the onset temperature of TR (48 K/min for the LG HG2 [21]). Lastly, T3 denotes the maximum surface temperature. In Fig. 12c, T1 occurred at an onset temperature of 347.69 K after 145 s of simulation. In the same figure, T2 had an onset temperature of 445.43 K at t = 1463.3 s, whereas T3 occurred 20 s later. Heat generation due to $\dot{Q}_{tot,H}$ starts to become the predominant heat source, as seen in Fig. 12b towards the onset temperature of T2. It is observed that $\dot{Q}_{tot,H}$ generates a significant amount of heat, leading to a fast temperature rise. The battery is damaged after T3, resulting in different thermophysical properties due to fire and explosions. Due to limitations in the model, changes in the LIB's thermophysical properties after T3 are not captured. Hence, the predicted temperature after T3 in Fig. 12c is due to the assumption of thermophysical and physicochemical properties.

To observe the predicted thermal response of the second battery (pouch) in simulation, a 6C discharge and charge cycle are simu-

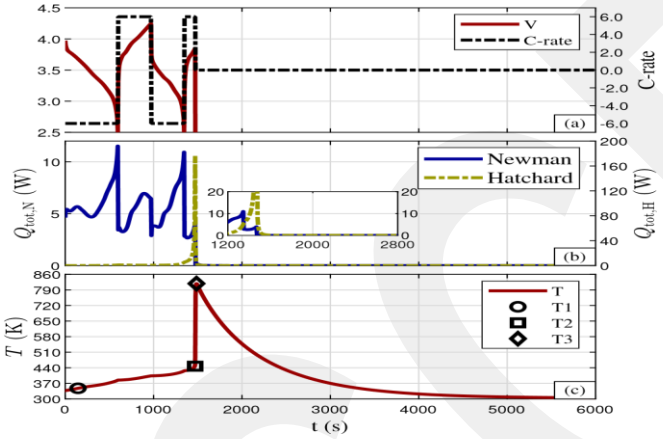

Figure 12: Predictions of working voltage, heat generation rate, and surface temperature variation over time. Current rate: 6C, initial temperature: 338.15 K, ambient temperature: 303.15 K. T1: heat rate of 0.02 K/min, T2: TR onset temperature, T3: maximum temperature.

lated. The model is cycled between 2.5 V and 3.8 V until TR occurs. The ambient and battery temperatures are set to 338.15 K in this test, and the thermophysical and physicochemical properties of the model are assumed to be unchanged. Figure 13 displays the model's voltage, heat generation, and temperature prediction during simulation over time. The temperature predicted in Fig.13c rises from 338.15 K to 665.75 K in 3010 s.

Assuming that different stages of decomposition start when the temperature rate reaches 0.02 K/min [33] for different layers. The onset temperature of the SEI is predicted to be 383.57 K, from the simulation result. This condition occurs after 550 s of simulation. The negative-solvent reaction starts 135 s later at 392.85 K. The onset temperature for the positive-solvent occurs when the temperature reaches 419.65 K, at t = 1355 s, whereas the electrolyte decomposition starts at 510.15 K at t = 2815 s as seen in Fig. 13c. Heat generation due to $Q_{tot,H}$ starts to become the predominant heat source, as seen in Fig. 13b towards the onset temperature of the electrolyte. From the simulation, it can be observed that after the onset temperature of the electrolyte, $Q_{tot,H}$ generates 3.4 times more heat than $Q_{tot,N}$, leading to a fast temperature rise. The heat rate above 1 K/min, representing the TR's onset temperature [33] is predicted at 540.25 K. The LIB gets damaged after TR, resulting in different thermophysical properties due to fire and explosions.

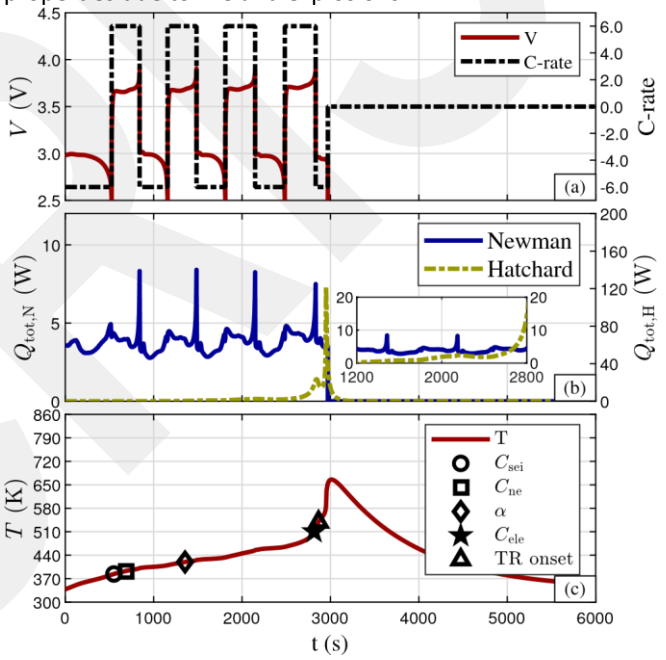

Figure 13: Simulation prediction for voltage, heat generation, and temperature variation over time. Current rate: 6C, initial temperature: 338.15 K, ambient temperature: 338.15 K. Decomposition of SEI: C_{sei}, negative-solvent reaction: C_{ne}, positive-solvent reaction: α, electrolyte decomposition: C_{ele}.

10. Conclusions

Declaration of Competing Interest

The authors declare that they have no known competing financial interests or personal relationships that could have appeared to influence the work reported in this paper.

References

[1] IEA – International Energy Agency, iea.org, accessed: 2023-08-24.

[2] Y. Li, X. Gao, X. Feng, D. Ren, Y. Li, J. Hou, Y. Wu, J. Du, L. Lu, M. Ouyang, Battery eruption triggered by plated lithium on an anode during thermal runaway after fast charging, Energy 239 (2022) 122097. doi:10.1016/j.energy.2021.122097.

[3] J. Liu, Z. Wang, J. Bai, T. Gao, N. Mao, Heat generation and thermal runaway mechanisms induced by overcharging of aged lithium-ion battery, Applied Thermal Engineering 212 (2022) 118565. doi:10.1016/j.applthermaleng.2022.118565.

[4] J. Hu, T. Liu, X. Wang, Z. Wang, L. Wu, Investigation on thermal runaway of 18,650 lithium ion battery under thermal abuse coupled with charging, Journal of Energy Storage 51 (2022) 104482. doi:10.1016/j.est.2022.104482.

[5] O. Dongxu, C. Mingyi, H. Que, W. Jingwen, W. Zhi, W. Jian, A review on the thermal hazards of the lithium-ion battery and the corresponding countermeasures, Applied Sciences 9 (12) (2019) 2483. doi:10.3390/app9122483.

[6] Z. Yang, Y. Yan, U. Pak, Thermal reliability assessment and sensitivity analysis of 18,650 cylindrical lithium–ion battery, Journal of Energy Storage 59 (2023) 106504. doi:10.1016/j.est.2022.106504.

[7] X. Yu, R. Chen, L. Gan, H. Li, L. Chen, Battery safety: From lithium-ion to solid-state batteries, Engineering 21 (2023) 9–14. doi:10.1016/j.eng.2022.06.022.

[8] M. Doyle, J. Newman, A. S. Gozdz, C. N. Schmutz, J.-M. Tarascon, Comparison of modeling predictions with experimental data from plastic lithium ion cells, Journal of The Electrochemical Society 143 (6) (1996) 1890–1903. doi:10.1149/1.1836921.

[9] M. Alipour, E. Esen, R. Kizilel, Investigation of 3-d multilayer approach in predicting the thermal behavior of 20 ah li-ion cells, Applied Thermal Engineering 153 (2019) 620–632. doi:10.1016/j.applthermaleng.2019. 03.020.

[10] C. Li, H. Zhang, R. Zhang, Y. Lin, H. Fang, On the characteristics analysis and tab design of an 18650 type cylindrical $LiFePO_4$ battery, Applied Thermal Engineering 182 (2021) 116144. doi:10.1016/j.applthermaleng.2020.116144.

[11] R. Rania, L. Hasna, G. Hamid, S. Pierre, A. Guven, Experimental analysis on li-ion battery local heat distribution, Journal of Thermal Analysis and Calorimetry 138 (2) (2019) 1557–1571. doi:10.1007/ s10973-019-08283-9.

[12] Z. Khalid, L. Hasna, P. Rafaele, G. Hamid, S. Pierre, Experimental investigation on the impact of the battery charging/discharging current ratio on the operating temperature and heat generation, International Journal of Energy Research 45 (11) (2021) 16754–16768. doi:10.1002/er.6923.

[13] L. Boxia, Z. Wenjiao, Z. Carlos, U. Nils, R. Magnus, S. H. Jurgen, Ex-¨ perimental analysis of thermal runaway in 18650 cylindrical li-ion cells using an accelerating rate calorimeter, Batteries 3 (2) (2017). doi:10.3390/batteries3020014.

[14] J. Chen, X. Rui, H. Hsu, L. Lu, C. Zhang, D. Ren, L. Wang, X. He, X. Feng, M. Ouyang, Thermal runaway modeling of $LiNi_{0.6}Mn_{0.2}Co_{0.2}O_2$/graphite batteries under different states of charge, Journal of Energy Storage 49 (2022) 104090. doi:10.1016/j.est.2022.104090.

[15] T. T. D. Nguyen, S. Abada, A. Lecocq, J. Bernard, M. Petit, G. Marlair, S. Grugeon, S. Laruelle, Understanding the thermal runaway of ni-rich lithium-ion batteries, World Electric Vehicle Journal 10 (4) (2019). doi:10.3390/wevj10040079.

[16] H. Chen, J. E. H. Buston, J. Gill, D. Howard, R. C. E. Williams, E. Read, A. Abaza, B. Cooper, J. X. Wen, A simplified mathematical model for heating-induced thermal runaway of lithium-ion batteries, Journal of The Electrochemical Society 168 (2021) 010502. doi:10.1149/1945-7111/abd64c.

[17] C. Jin, Y. Sun, H. Wang, Y. Zheng, S. Wang, X. Rui, C. Xu, X. Feng, H. Wang, M. Ouyang, Heating power and heating energy effect on the thermal runaway propagation characteristics of lithium-ion battery module: Experiments and modeling, Applied Energy 312 (2022) 118760. doi:10.1016/j.apenergy.2022.118760.

[18] H. Li, D. Zhou, M. Zhang, B. Liu, C. Zhang, Multi–field interpretation of internal short circuit and thermal runaway behavior for lithium–ion batteries under mechanical abuse, Energy 263 (2023) 126027. doi:10.1016/j.energy.2022.126027.

[19] K. Suhwan, S. Jihun, L. Hyobin, J. Seungwon, P. Joonam, L. Hongkyung, L. Y. Min, Simulation study on internal short circuits in a li-ion battery depending on the sizes, quantities, and locations of li dendrites, Frontiers in Materials 9 (2022). doi:10.3389/fmats.2022.850610.

[20] T. G. Tranter, R. Timms, T. M. M. Heenan, S. G. Marquis, V. Sulzer, A. Jnawali, M. D. R. Kok, C. P. Please, S. J. Chapman, P. R. Shearing, D. J. L. Brett, Probing heterogeneity in li-ion batteries with coupled multiscale models of electrochemistry and thermal transport using tomographic domains, Journal of The Electrochemical Society 167 (11) (2020) 110538. doi:10.1149/1945-7111/aba44b.

[21] T. T. D. Nguyen, Understanding and modelling the thermal runaway of li-ion batteries, Ph.D. thesis, Universite de Picardie Jules Verne (2021).´

[22] L. O. Valøen, J. N. Reimers, Transport properties of $LiPF_6$-based liion battery electrolytes, Journal of The Electrochemical Society 152 (5) (2005) A882. doi:10.1149/1.1872737.

[23] Y. Xing-Yan, P. Michael, Tab design and failures in cylindrical li-ion batteries, IEEE-Access 7 (2019) 24082–24095. doi:10.1109/ACCESS.2019.2899793.

[24] M. Alipour, L. Yin, S. S. Tavallaey, A. M. Andersson, D. Brandell, A surrogate-assisted uncertainty quantification and sensitivity analysis on a coupled electrochemical–thermal battery aging model, Journal of Power Sources 579 (2023) 233273. doi:10.1016/j.jpowsour.2023.233273.

[25] C.-H. Chen, F. B. Planella, K. O'Regan, D. Gastol, W. D. Widanage, E. Kendrick, Development of experimental techniques for parameterization of multi-scale lithium-ion battery models, Journal of The Electrochemical Society 167 (8) (2020) 080534. doi:10.1149/1945-7111/ ab9050.

[26] A. Nyman, M. Behm, G. Lindbergh, Electrochemical characterisation and modelling of the mass transport phenomena in $LiPF_6$–EC–EMC electrolyte, Electrochimica Acta 53 (22) (2008) 6356–6365. doi:10.1016/j.electacta.2008.04.023.

[27] T. D. Hatchard, D. D. MacNeil, A. Basu, J. R. Dahn, Thermal model of cylindrical and prismatic lithium-ion cells, Journal of The Electrochemical Society 148 (7) (2001) A755. doi:10.1149/1.1377592.

[28] D. Bernardi, E. Pawlikowski, J. Newman, A general energy balance for battery systems, Journal of The Electrochemical Society 132 (1) (1985) 5. doi:10.1149/1.2113792.

[29] M. Xu, Z. Zhang, X. Wang, L. Jia, L. Yang, A pseudo three-dimensional electrochemical–thermal model of a prismatic $LiFePO_4$ battery during discharge process, Energy 80 (2015) 303–317. doi:10.1016/j.energy.2014.11.073.

[30] J. Sturm, A. Rheinfeld, I. Zilberman, F. Spingler, S. Kosch, F. Frie, A. Jossen, Modeling and simulation of inhomogeneities in a 18650 nickel-rich, silicon-graphite lithium-ion cell during fast charging, Journal of Power Sources 412 (2019) 204–223. doi:10.1016/j.jpowsour.2018.11.043.

[31] F. Jiang, P. Peng, Y. Sun, Thermal analyses of $LiFePO_4$/graphite battery discharge processes, Journal of Power Sources 243 (2013) 181–194. doi:10.1016/j.jpowsour.2013.05.089.

[32] S. Abada, M. Petit, A. Lecocq, G. Marlair, V. Sauvant-Moynot, F. Huet, Combined experimental and modeling approaches of the thermal runaway of fresh and aged lithium-ion batteries, Journal of Power Sources 399 (2018) 264–273. doi:10.1016/j.jpowsour.2018.07.094.

[33] P. J. Bugryniec, J. N. Davidson, D. J. Cumming, S. F. Brown, Pursuing safer batteries: Thermal abuse of $LiFePO_4$ cells, Journal of Power Sources 414 (2019) 557–568. doi:10.1016/j.jpowsour.2019.01.013.

[34] P. Peng, S. Yiqiong, , J. Fangming, Thermal analyses of $LiCoO_2$ lithiumion battery during oven tests, Heat and Mass Transfer 50 (10) (2014) 1405–1416. doi:10.1007/s00231-014-1353-x.

[35] X. Feng, M. Ouyang, X. Liu, L. Lu, Y. Xia, X. He, Thermal runaway mechanism of lithium ion battery for electric vehicles: A review, Energy Storage Materials 10 (2018) 246–267. doi:10.1016/j.ensm.2017.05.013.

[36] G.-H. Kim, A. Pesaran, R. Spotnitz, A three-dimensional thermal abuse model for lithium-ion cells, Journal of Power Sources 170 (2) (2007) 476–489. doi:10.1016/j.jpowsour.2007.04.018.

[37] Y. Huang, Y. Wu, B. Liu, Experimental investigation into the use of emergency spray on suppression of battery thermal runaway, Journal of Energy Storage 38 (2021) 102546. doi:10.1016/j.est.2021.102546.

[38] P. T. Coman, E. C. Darcy, C. T. Veje, R. E. White, Numerical analysis of heat propagation in a battery pack using a novel technology for triggering thermal runaway, Applied Energy 203 (2017) 189–200. doi:10.1016/j.apenergy.2017.06.033.

[39] X. Feng, X. He, M. Ouyang, L. Wang, L. Lu, D. Ren, S. Santhanagopalan, A coupled electrochemical-thermal failure model for predicting the thermal runaway behavior of lithium-ion batteries, Journal of The Electrochemical Society 165 (16) (2018) A3748. doi:10.1149/2.0311816jes.

[40] P. T. Coman, E. C. Darcy, C. T. Veje, R. E. White, Modelling li-ion cell thermal runaway triggered by an internal short circuit device using an efficiency factor and arrhenius formulations, Journal of The Electrochemical Society 164 (4) (2017) A587. doi:10.1149/2.0341704jes.

[41] A. V. Shelke, J. E. Buston, J. Gill, D. Howard, K. C. Abbott, S. L. Goddard, E. Read, G. E. Howard, A. Abaza, B. Cooper, J. X. Wen, Characterizing and predicting 21700 NMC lithium-ion battery thermal runaway induced by nail penetration, Applied Thermal Engineering 209 (2022) 118278. doi:10.1016/j.applthermaleng.2022.118278.

[42] P. J. Bugryniec, J. N. Davidson, S. F. Brown, Computational modelling of thermal runaway propagation potential in lithium iron phosphate battery packs, Energy Reports 6 (2020) 189–197. doi:10.1016/j.egyr.2020. 03.024.

[43] Z. Jia, Z. Huang, H. Zhai, P. Qin, Y. Zhang, Y. Li, Q. Wang, Experimental investigation on thermal runaway propagation of 18,650 lithium-ion battery modules with two cathode materials at low pressure, Energy 251 (2022) 123925. doi:10.1016/j.energy.2022.123925.

[44] R. Pakrouh, M. Hosseini, R. Bahrampoury, A. Ranjbar, S. Borhani, Cylindrical battery thermal management based on microencapsulated phase change slurry, Journal of Energy Storage 40 (2021) 102602. doi:10.1016/j.est.2021.102602.

[45] Dunya geneli s¸ehirlerde iklim verileri,¨ tr.climate-data.org, accessed: 2023-08-21.

[46] O. Willstrand, M. Pushp, P. Andersson, D. Brandell, Impact of different liion cell test conditions on thermal runaway characteristics and gas release measurements, Journal of Energy Storage 68 (2023) 107785. doi:10.1016/j.est.2023.107785.